Structural and compositional diversity in the kainate receptor family

Purushotham Selvakumar[1,5], **Joon Lee**[2,5], **Nandish Khanra**[1], **Changhao He**[1], **Hermany Munguba**[2], **Lisa Kiese**[3], **Johannes Broichhagen**[4], **Andreas Reiner**[3], **Joshua Levitz**[2,*], **Joel R. Meyerson**[1,6,*]

[1]Department of Physiology and Biophysics, Weill Cornell Medical College, New York, NY 10065, USA

[2]Department of Biochemistry, Weill Cornell Medical College, New York, NY 10065, USA

[3]Department of Biology and Biotechnology, Ruhr University Bochum, Bochum, Germany

[4]Leibniz-Forschungsinstitut für Molekulare Pharmakologie, 13125 Berlin, Germany

[5]These authors contributed equally

[6]Lead contact

SUMMARY

The kainate receptors (KARs) are members of the ionotropic glutamate receptor family and assemble into tetramers from a pool of five subunit types (GluK1–5). Each subunit confers distinct functional properties to a receptor, but the compositional and stoichiometric diversity of KAR tetramers is not well understood. To address this, we first solve the structure of the GluK1 homomer, which enables a systematic assessment of structural compatibility among KAR subunits. Next, we analyze single-cell RNA sequencing data, which reveal extreme diversity in the combinations of two or more KAR subunits co-expressed within the same cell. We then investigate the composition of individual receptor complexes using single-molecule fluorescence techniques and find that di-heteromers assembled from GluK1, GluK2, or GluK3 can form with all possible stoichiometries, while GluK1/K5, GluK2/K5, and GluK3/K5 can form 3:1 or 2:2 complexes. Finally, using three-color single-molecule imaging, we discover that KARs can form tri- and tetra-heteromers.

Graphical Abstract

In brief

Selvakumar et al. use cryo-electron microscopy, single-cell RNA sequencing analysis, and single-molecule fluorescence techniques to investigate the stoichiometric and assembly diversity of kainate receptors (KARs). The work gives insight into KAR molecular diversity and expands the potential KAR subunit combinations to include a variety of di-, tri-, and tetra-heteromers.

INTRODUCTION

Kainate receptors (KARs) are members of the iGluR family, which can either localize post-synaptically to drive synaptic depolarization or pre-synaptically to regulate neurotransmitter release (Contractor et al., 2011; Lerma and Marques, 2013; Reiner and Levitz, 2018). KARs are tetrameric channels that assemble from five subunit types (GluK1–5). GluK1, GluK2, and GluK3 share ~75% identity (Table S1) and can form functional homo-tetramers (homomers) on their own or can co-assemble with any other KAR subunit to form hetero-tetramers (heteromers) (Cui and Mayer, 1999; Mulle et al., 2000; Pinheiro et al., 2007; Pollok and Reiner, 2020; Veran et al., 2012). In contrast to GluK1–3, GluK4 and GluK5 are obligate heteromer subunits, which must co-assemble into tetramers with GluK1–3 to function (Herb et al., 1992; Werner et al., 1991). GluK4 and GluK5 share ~70% sequence identity but only ~40% with GluK1–3 (Table S1). Understanding assembly patterns is critical to KAR biology as heteromers are likely the primary KARs in the brain (Herb et

al., 1992; Petralia et al., 1994; Werner et al., 1991), with unique heteromeric combinations providing a means to fine-tune KAR functional properties.

In recent years structures of GluK2 and GluK3 homomers and a GluK2/K5 heteromer (Khanra et al., 2021; Kumari et al., 2019; Meyerson et al., 2014a, 2016) visualized how the amino terminal domains (ATDs), ligand binding domains (LBDs), and transmembrane domains (TMDs) are arranged within the tetrameric receptor complexes. However, our understanding of KAR composition and subunit compatibility has been largely driven by electro-physiological and biophysical studies investigating KAR homomers and KAR di-heteromers (i.e., tetramers composed of two different subunit types). Di-heteromers of GluK1, GluK2, or GluK3 form functional channels, but their stoichiometries are un-clear (Cui and Mayer, 1999; Pollok and Reiner, 2020; Veran et al., 2012). GluK2/K5 di-heteromers are reported to harbor two copies of each subunit type (2:2 ratio) (Khanra et al., 2021; Litwin et al., 2020; Reiner et al., 2012), although whether other stoichiometries are possible is not known. It is also unknown if heteromers having more than two subunit types may form, as has been seen with the other iGluRs, the NMDA (Paoletti et al., 2013) and AMPA receptors (Zhao et al., 2019).

The physiological spectrum of KAR tetramer compositions is constrained by the degree of subunit co-expression within a given cell. KAR subunit abundance in the brain has been investigated using *in situ* hybridization (Bahn et al., 1994; Paternain et al., 2000; Wisden and Seeburg, 1993; Wyeth et al., 2017) or immunohistochemistry (Hadzic et al., 2017; Petralia et al., 1994), but these methods lack sufficient precision for a quantitative analysis of subunit co-expression. As such, our ability to define the feasibility of different KAR combinations *in vivo* has been limited, motivating higher resolution KAR expression analysis to complement and guide structural and biophysical studies.

In this study, we aim to answer three key questions. First, do the structural and conformational attributes of KAR subunits prohibit the formation of di-heteromers with particular stoichiometries or tri- or tetra-heteromers? Second, what are the KAR subunit expression patterns in single neurons, and do they make the formation of varied KAR di-heteromers or KAR tri- and tetra-heteromers plausible? Third, what are the stoichiometries of KAR heteromers? We investigate these questions using a combination of cryo-electron microscopy (cryo-EM), single-cell RNA sequencing (scRNA-seq), single-molecule pull-down (SiMPull), and single-molecule Förster resonance energy transfer (smFRET). Together, our analyses reveal the extent of molecular diversity among KARs and substantially expand the repertoire of potential KAR subunit combinations to include a variety of di-, tri-, and tetra-heteromers.

RESULTS

Structure of the full-length GluK1 homomer and comparison of full-length KAR structures

To enable a more comprehensive structural analysis of KARs, GluK1 was expressed, purified, and the structure solved by cryo-EM with saturating L-Glu (1 mM) (Figures 1A, S1, and S2). We first analyzed the KAR ATDs because they are thought to encode the subunit compatibility logic during receptor biogenesis and, thus, the propensity for

various homomers and heteromers to form (Zhao et al., 2017). Analysis was performed with ATD layers from full-length GluK1, GluK2, GluK3, and GluK2/K5 structures (Khanra et al., 2021; Kumari et al., 2019; Meyerson et al., 2016). ATD monomer conformations were evaluated using GluK1 as a reference and by aligning GluK2, GluK3, and GluK5 to it. Alignment to the GluK1 ATD was further restricted to the R1 domain (upper lobe), which had the effect of magnifying conformational differences in the R2 domain (lower lobe) and thereby aided visualization. After alignment, each ATD monomer was colored according to its measured root-mean-square deviation (RMSD) with respect to the entire GluK1 monomer (Figure 1B). This analysis showed that the GluK1 ATD conformation is most similar to GluK3, followed closely by GluK2, and diverges from the conformation of GluK5 (Kumar and Mayer, 2010).

Similar analysis was done with ATD homodimers, where one subunit of the GluK1 ATD dimer was used as a reference to align GluK2 and GluK3 ATDs (Figure 1C, gray subunits). This allowed for RMSD visualization of the second subunit in each dimer pair (Figure 1C, cyan/magenta subunits). The visualization revealed that inter-domain conformational difference within ATD dimers for GluK1–3 is modest, with little change in the average RMSD value or in RMSD coloring (Figure 1C) relative to the monomer analysis (Figure 1B). However, as expected from the monomer analysis of GluK5 (Figure 1B), in a dimeric context GluK5 again shows clear conformational differences with GluK1 (Figure 1C), and based on RMSD coloring, the differences are most pronounced at the periphery of both lobes of the GluK5 subunit.

We assessed conformational differences between ATD tetramer layers for GluK1, GluK2, GluK3, and GluK2/K5 by measuring the angle formed between ATD dimers at the dimer-dimer interface (Figure 1D). The angle was measured from the C-terminal tip of helix 8 on the peripheral ATDs (A/C subunits) to the dimer-dimer interface (Figure 1D, white annotation). This yielded similar angles of 171°, 171°, 169°, and 166° for GluK1, GluK2, GluK3, and GluK2/K5, respectively. A sequence alignment between regions that formed the interface between ATD dimers showed nearly complete conservation in GluK1–3 (Figure 1E). Overall, the conformational analysis of KAR ATDs showed that GluK1–3 had a high degree of conformational similarity, with average RMSD values ranging from ~1 to 2 Å (Figures 1B and 1C). We conclude that there is not a significant conformational difference between ATD layers of GluK1–3, supporting a hypothesis that the subunits can assemble promiscuously and that each can occupy any of the four "slots" in a KAR heteromer. Furthermore, there appears to be no obvious structural features that would prevent GluK5 from occupying only one slot rather than always two slots, as is presently thought (Khanra et al., 2021; Kumar et al., 2011; Reiner et al., 2012).

GluK1 was visualized with saturating L-Glu, but the resolution in the LBDs was insufficient to resolve ligands (Figures S2C and S2J). We inferred L-Glu occupancy in the LBDs by comparing the cryo-EM density to high-resolution crystal structures of isolated LBDs (Figure S2K). Comparison of the GluK1 LBD tetramer layer with that from GluK2, GluK3, and GluK2/K5 showed that the structures had a similar arrangement with low RMSD values (Figures 1F–1I). The LBD arrangements all formed ring-like motifs centered around the

receptor central axis and mediated by G helices in the LBD subunits (Figures 1F–1I, yellow highlights), showing their overall structure is consistent between the KAR structures.

scRNA-seq analysis reveals complex co-expression patterns of KAR subunits

We next aimed to quantify the stoichiometries of GluK1, GluK2, GluK3, and GluK5 di-heteromers, probe where subunits are positioned within di-heteromers and determine whether tetramers having more than two subunit types are possible (e.g., GluK1/K2/K5 tri-heteromer or GluK1/K2/K3/K5 tetra-heteromer). However, we first considered which KAR subunit types may co-assemble together in single neurons under physiological conditions.

To quantitatively define KAR subunit co-expression patterns, we turned to scRNA-seq, which provides transcriptome measurement at the single-cell level (Poulin et al., 2016) and made use of a transcriptomic dataset from ~10,000 cells from the mouse frontal cortex (anterior lateral motor cortex) (Tasic et al., 2018). We analyzed KAR expression in glutamatergic neurons, GABAergic neurons, and non-neuronal cells, which can each be further divided into subclasses. All five KAR subunit genes (*Grik1–5*) were observed across subclasses (Figure S3A). *Grik2–5* showed substantial levels across glutamatergic neurons, although *Grik3* was mostly excluded from layer 2/3 and layer 5 intra-telencephalic (IT) neurons (Figure 2A). *Grik1* was primarily expressed across GABAergic interneurons and the near-projecting (NP) subclass of glutamatergic neurons (Figure 2A). *Grik2* also showed broad expression across GABAergic neurons, while *Grik3, Grik4*, and *Grik5* showed expression in only a subset including somatostatin (Sst)-expressing interneurons (Figure 2A). KAR expression in non-neuronal cells was substantially lower than in neurons, but clear expression was observed in subsets of cells, including astrocytes and oligodendrocytes for both *Grik1* and *Grik2* (Figure 2A). For a broad overview of KAR co-expression, we analyzed the proportion of neurons showing expression of two or more KAR subunit types. We performed this analysis with various cut-offs of RNA reads per cell measured in counts per million (CPMs). Strikingly, we found up to four KAR subunits co-expressed per cell depending on the cutoff. Using a 5 CPM cutoff, 50% of glutamatergic neurons expressed more than ~3.2 KAR subunit types, and 50% of GABAergic neurons expressed more than ~3.5 KAR subunit types (Figure 2B). This indicates co-expression of multiple subunit types likely occurs in the vast majority of cortical neurons and that the molecular diversity of KARs is slightly higher in GABAergic than glutamatergic neurons.

To better understand KAR subunit-type co-expression, we performed pairwise analysis of each subunit combination across all neuronal subclasses using a 5 CPM cutoff (Lee et al., 2020). The analysis (Figures 2C and S3B) shows highly variable fractions of co-expressing cells depending on the KAR subunit type and cell subclass. For example, in the L2/3 IT subclass, 78% of cells show *Grik2/5* co-expression, 57% show *Grik2/4* co-expression, and none show *Grik1/2* co-expression. An especially high degree of co-expression was seen in GABAergic subclasses, including in Sst interneurons where all pairs other than those containing *Grik4* show >65% co-expression (Figure 2C). Cell-by-cell scatterplots of co-expression reveal a wide range of RNA ratios for each subunit pair (Figure S3C). For example, while *Grik1* and *Grik2* show co-expression in 79% of Sst interneurons (Figure 2C), the ratio of RNA molecules can range from 100:1 to 1:100 *Grik1:Grik2* (Figure S3C).

Given the wide range of expression ratios observed between *Grik1* and other subtypes in Sst interneurons (Figure S3C), we asked if this variability was due to cell-by-cell differences or to distinct expression properties across Sst interneuron subtypes. To assess this, we plotted the expression ratios for *Grik1* across six distinct subtypes of Sst interneurons (Figure S3D) (Göngrich et al., 2020; Hilscher et al., 2017; Ma et al., 2006; Muñoz et al., 2017; Naka et al., 2019; Tasic et al., 2018). While subtle differences were observed in different Sst subtypes, including a clear bias toward higher *Grik1* expression in the Chodl Sst interneurons, the generally broad profile of expression ratios was maintained across Sst subtypes. This indicates that analysis at the level of broad cell subclasses captures the diversity of KAR expression properties and that variability in expression levels is primarily a cell-by-cell feature rather than a property of different cellular subtypes.

Given the clear co-expression of more than two KAR subunit types in many neurons, we analyzed the proportion of cells showing a single subunit type and all possible subunit pairs, as well as all combinations of three or four subunits (Figure 2D). Few cell subclasses showed a substantial population of cells with only one KAR subunit type, with the exception of *Grik2* in a subset of layer 5 IT neurons and GABAergic neurons. In contrast, many cell subclasses showed expression of three KAR subunit types, including a wide variety of combinations in glutamatergic neurons and frequent co-expression of *Grik1*, *Grik2*, and *Grik5* in parvalbumin (Pvalb)-expressing and Sst interneurons (Figures 2D and S3D). Comparison of expression ratios across *Grik1*, *Grik2*, and *Grik5* show diversity in relative co-expression properties with primarily *Grik2/5* co-expression in L2/3 IT neurons and co-expression of all three subtypes in Sst and Pvalb interneurons (Figure 2E). Finally, a subset of neuron subclasses show expression of four KAR subunit types, with the most prominent examples being *Grik1/2/3/5* co-expression in Sst interneurons and *Grik2/3/4/5* co-expression in many glutamatergic neurons (Figure 2D).

Defining the stoichiometry and subunit arrangement of KAR di-heteromers

Having established the general structural compatibility (Figure 1) and extensive co-expression of KAR subunit types (Figure 2), we aimed to assess the assembly, stoichiometry, and subunit arrangement of KARs composed of different pairs of subunit types, starting with di-heteromers. We employed the SiMPull method in which detergent-solubilized and fluorophore-tagged receptors are immobilized via antibodies and their subunits counted by photobleaching step analysis (Jain et al., 2011; Lee et al., 2020; Levitz et al., 2016; Royal et al., 2019; Thibado et al., 2021). We first generated GluK1 and GluK2 constructs with an N-terminal hemagglutinin (HA) epitope followed by a SNAP tag (Figure S4B) amenable to labeling with organic dyes, and both maintained normal receptor function (Figure S4B; Table S2).

To establish the viability of our experimental system, we used SiMPull to detect KAR homo-tetramers. We labeled cells expressing HA-SNAP-GluK1 or HA-SNAP-GluK2 with Oregon Green ("OG") fluorophores conjugated to a membrane-impermeant sulfonated benzylguanine ("SBG") group for SNAP-tag conjugation (Poc et al., 2020). Cells were lysed, receptors immobilized, and single molecules were imaged with total internal reflection fluorescence microscopy (Figures 3A and 3B). Up to four bleaching steps were

observed per molecule with a range of one to four steps per molecule in distributions consistent with a strict tetramer (Figure 3C).

To assess the positions of subunits within KAR tetramers, we used smFRET (Lerner et al., 2021; Roy et al., 2008). Based on the relative distances between ATDs within a tetramer, we reasoned that interaction between ATD dimers, but not between other subunit pairs, would be detected by fluorophores with a Förster radius of ~6 nm (Roy et al., 2008) (Figure 3D). We thus hypothesized that FRET would only generate a signal for subunits associated within an ATD dimer (i.e., A/B or C/D subunit pairs), yielding smFRET histograms with a single peak. We labeled HA-SNAP-GluK1 or HA-SNAP-GluK2 with a mix of benzylguanine (BG) donor (BG-LD555) and acceptor (BG-LD655) fluorophores and observed FRET in a subset of molecules (Figure 3E). Representative single-molecule traces (Figures 3E, S4D, and S4E) showed stable FRET levels of ~0.2 to 0.3 for the entire recording, and, accordingly, smFRET histograms showed single peaks centered at 0.2 (GluK1) or 0.3 (GluK2) (Figure 3F).

To enable investigation of GluK1/K2 di-heteromers, we generated a GluK2 construct with an N-terminal FLAG epitope followed by a CLIP tag for attachment to benzylcytosine-conjugated (BC) fluorophores. To analyze GluK1/K2 di-heteromers, we co-expressed HA-SNAP-GluK1 and FLAG-CLIP-GluK2 at either a 10:1 or 1:10 DNA ratio and labeled cells with SBG-OG and BC-DY547 fluorophores prior to lysis (Figure S4H). Receptors were immobilized via anti-HA antibodies, and fluorescence co-localization indicated di-heteromers (Figure 3G). Bleaching step analysis of each co-localized spot revealed 1, 2, or 3 three steps for either GluK1 or GluK2 subunits within a heteromer (Figures 3H and 3I). smFRET experiments using a BG-conjugated donor (BG-LD555) for SNAP-GluK1 and BC-conjugated acceptor (BC-LD655) for CLIP-GluK2 (Figure 3J) showed stable FRET (Figure S4M) and a histogram with a single peak of ~0.25 (Figures 3J and 3K), providing evidence of heteromerization within the ATD dimers. Together, these experiments show that GluK1/K2 hetero-tetramers form readily with all possible configurations (Figure 3L).

We next investigated the class of KAR di-heteromers that form between the GluK1–3 and GluK4–5 subfamilies. We fused GluK2 and GluK5 with an N-terminal Halo-tag (Figure S5A), which recognizes chloroalkane (CA)-conjugated fluorophores, and preserved normal receptor function (Figure S5B). To again limit labeling to surface receptors, we used modified sulfonated rhodamine fluorophores ("Sulfo549"), which are bright and membrane-impermeable (Birke et al., 2021). We then co-expressed either HA-SNAP-GluK1 or HA-SNAP-GluK2 with Halo-GluK5 at either a 1:1 or 1:10 DNA ratio and labeled with SBG-OG and CA-Sulfo549 (Figure S5E). Upon immobilization of receptors via the anti-HA antibody, many co-localized spots were observed (Figures 4A and 4B) and distinct photobleaching step distributions were observed for GluK1 and GluK2 versus GluK5, in contrast to GluK1/K2 di-heteromers where the subunits showed the same distributions. Both HA-SNAP-GluK1 and HA-SNAP-GluK2 showed up to three subunits per complex with a larger proportion with the 1:1 DNA ratio, while Halo-GluK5 showed almost exclusively one- and two-step behaviors (Figures 4C and 4D). This indicates that 3:1 and 2:2 GluK1:GluK5 or GluK2:GluK5 heteromers can form but not 1:3.

Our SiMPull data showing 3:1 GluK1:GluK5 and GluK2:GluK5 di-heteromers presents an apparent contradiction with prior single-molecule imaging and structural studies, which reported a strict 2:2 stoichiometry (Khanra et al., 2021; Kumar et al., 2011; Reiner et al., 2012). However, heteromer stoichiometry is sensitive to expression conditions, and 3:1 di-heteromers are more pronounced with higher GluK1:GluK5 and GluK2:GluK5 expression ratios (Figures 4C, 4D, S5G, and S5H), which were not previously tested. We used smFRET to test our hypothesis that GluK2/K5 and GluK1/K5 heterotetramers harbor homodimers and heterodimers within the ATD. When we expressed HA-Halo-GluK5 and CLIP-GluK2 at a 1:10 ratio then labeled CLIP-tags with a mix of donor (BC-LD555) and acceptor (BC-LD655) fluorophores and immobilized heteromers via the anti-HA antibody, robust smFRET was observed with an average value of ~0.2, indicating that GluK2 ATD homodimers can form within GluK2/K5 heterotetramers (Figure 4E). In addition, clear smFRET (average value ~0.3) was observed between donor/acceptor-labeled HA-SNAP-GluK5 and CLIP-GluK2 subunits (Figure 4F), confirming ATD heterodimers. In contrast, smFRET was not observed between HA-SNAP-GluK5 subunits, which is expected based on the knowledge that GluK5 can only occupy the peripheral (A/C) positions on the ATD layer (Figure 4G) (Khanra et al., 2021; Kumar et al., 2011).

KARs can form tri-heteromers and tetra-heteromers

To test for tri-heteromers, we identified three compatible fluorophores: SBG-OG (SNAP labeling; 488 nm excitation), BC-DY547 (CLIP labeling; 561 nm excitation) and CA-Sulfo646 (Halo labeling; 640 nm excitation). Co-expression at a 3:1:3 DNA ratio and fluorophore labeling of HA-SNAP-GluK1, FLAG-CLIP-GluK2, and Halo-GluK5 followed by SiMPull revealed a substantial population of spots co-localized in all three colors, providing clear evidence for tri-heteromerization (Figure 5A). Quantification showed ~10%–20% of each subunit type (average = 36/180 GluK2 subunits; 36/220 GluK5 subunits; 36/405 GluK1 subunits per movie) were found in GluK1/K2/K5 tri-heteromers. Similarly efficient tri-heteromer formation was observed when HA-Halo-GluK5 was used as the bait for imaging with SNAP-GluK1 and FLAG-CLIP-GluK2 (Figures S6D and S6E). Bleaching step analysis revealed that up to two bleaching steps could be observed for all subunit types within co-localized spots (Figures 5B and 5C) and restriction of our analysis to spots that showed a total of four bleaching steps confirmed that 2:1:1, 1:2:1 and 1:1:2 stoichiometries are all possible. With all findings considered we propose that GluK1/K2/K5 tri-heteromers can exist in 7 out of 18 possible configurations (Figure 5D).

We next asked if KAR tetra-heteromers containing four different subunit types can form. For this, we introduced GluK3 to our experimental system given its abundant co-expression with GluK1, GluK2, and GluK5 in somatostatin interneurons (SstINs) (Figure 2D). We first produced an HA-SNAP-GluK3 construct and confirmed homo-tetramerization after labeling with SBG-OG and immobilization (Figure S6F). We then co-expressed HA-SNAP-GluK3 with Halo-GluK2, Halo-GluK1, or Halo-GluK5 and observed many co-localized spots (Figures S6G–S6I). GluK3-containing di-heteromers showed similar bleaching step distributions to GluK1 and GluK2, with all stoichiometries observed for GluK1/K3 and GluK2/K3 di-heteromers and up to two GluK5 subunits in GluK3/K5 di-heteromers (Figures S6J–S6L).

Finally, we investigated the possibility that KARs can form tetra-heteromers composed of GluK1/K2/K3/K5. scRNA-seq analysis showed co-expression of these four subunits with 57.1% of Sst interneurons (650/1139 cells) and 21.2% of Pvalb interneurons (190/896 cells) expressing *Grik1*, *Grik2*, *Grik3*, and *Grik5* (Figure 2). To visualize tetra-tetramers, we co-expressed HA-GluK1 with SNAP-GluK3, FLAG-CLIP-GluK2, and Halo-GluK5 (Figure S6N) and immobilized spots via the anti-HA antibody (Figure 5E). This design enabled three-color imaging to detect tetra-heteromers based on each spot being immobilized by non-fluorescent GluK1. Conveniently, spots co-localized with only two colors enabled the detection of possible tri-heteromers (GluK1/K2/K3, GluK1/K2/K5, or GluK1/K3/K5), although double co-localized spots with one bleaching step in each color may either represent: (1) tri-heteromers with two GluK1 subunits (non-fluorescent), (2) tri-heteromers with incomplete labeling of the two visualized subtypes or (3) tetra-heteromers. However, by process of elimination, those spots with two fluorescent colors, and with two steps in one of the colors, must be tri-heteromeric. Extensive co-localization between immobilized spots was observed, including co-localization in two colors (tri-heteromers) or three colors (tetra-heteromers) (Figures 5F and 5G). For each subunit type, greater than 60% of molecules were co-localized with at least one other subunit and ~5% to 10% co-localized with two other subunits (Figure 5G). In conclusion, these data are consistent with a combination of di-, tri-, and tetra-heteromers formed upon co-expression of GluK1, GluK2, GluK3, and GluK5 (Figure 5H).

DISCUSSION

We employed structural biology (Figure 1) and scRNA-seq (Figure 2) to infer that KARs may form di-heteromers with balanced (2:2) and unbalanced (3:1, 1:3) stoichiometries and propose that tri- and tetra-heteromers may be possible. We tested these hypotheses with SiMPull and smFRET experiments on mature, surface-localized receptors (Figures 3, 4, and 5). We found that GluK1/K2, GluK2/K3, and GluK1/K3 can form di-heteromers with all possible stoichiometries and that their distributions depend on the expression level of each subunit (Figures 3 and 4). Investigations of GluK5 show di-heteromers with GluK1, GluK2, and GluK3 in a 2:2 ratio with GluK5 (Figures 4, S5, and S6). However, receptors harboring a single GluK5 subunit were also observed, revising the existing rules for GluK5 assembly (Kumar et al., 2011; Reiner et al., 2012). Although GluK4 was not investigated, it is thought to have the same assembly attributes as GluK5 (Zhao et al., 2017). Finally, we showed that KARs can form tri- and tetra-heteromers, indicating that KARs are at least as diverse as AMPA and NMDA receptors.

When our biophysical data are considered in the context of scRNA-seq data, we conclude that diverse heteromers are likely the rule rather than the exception, at least in the frontal cortex. The "high-affinity" GluK4 and GluK5 subunits have fundamentally different kinetic properties than GluK1–3 (Heckmann et al., 1996; Herb et al., 1992; Hollmann and Heinemann, 1994; Schiffer et al., 1997; Werner et al., 1991). In addition, KARs can undergo RNA splicing and editing (Herbrechter et al., 2021) and a plethora of subunit type-specific post-translational modifications including glycosylation (Vernon et al., 2017), phosphorylation (Wang et al., 1993), and ubiquitination (Maraschi et al., 2014). These sources of variability collectively enhance KAR capacity for functional fine-tuning. Going

forward, it will be important to extend single-molecule analysis to KARs *in situ* or isolated directly from mouse brain to define native heteromer populations, including receptor complexes with Neto proteins (Copits and Swanson, 2012; Tomita and Castillo, 2012), cytoplasmic proteins such as PSD95 (Garcia et al., 1998), and to C1ql2/Neurexin3 (Matsuda et al., 2016; Straub et al., 2016).

Limitations of the study

We note two salient limitations of the study. First, fluorescence experiments were done using recombinant expression in HEK293 cells, and non-physiological stoichiometries may have formed. However, considerable evidence suggests ATDs are the major arbiters of subunit compatibility for assembly (Ayalon and Stern-Bach, 2001; Duan et al., 2018; Zhao et al., 2017), and our constructs contain the ATD. Evidence also suggests that the ER quality-control mechanisms for KAR assembly are operational in heterologous expression systems including cells used in our study (Nasu-Nishimura et al., 2006; Reiner et al., 2012; Ren et al., 2003). This argues that although the precise statistics for each heteromer configuration may not precisely reflect the native proportions, the diverse range of heteromers we observe are likely found in neurons. Indeed, scRNA-seq data show all subunit combinations tested in our study are co-expressed in neurons (Figure 2). Second, we did not functionally assay different di-, tri-, or tetra-heteromers. However, electro-physiological measurements of heterologously expressed di-heteromers containing GluK1–3 show properties varying from cell to cell, indicating the expression of variable receptor populations (Cui and Mayer, 1999; Pollok and Reiner, 2020). Our results imply that the heteromers recorded in these experiments may have included a combination of 3:1, 2:2, and 1:3 stoichiometries. The structural and compositional results we present should motivate future investigation of distinct gating properties that may arise from the varied KAR complexes and their sensitivity to subtype-specific compounds.

STAR★METHODS

RESOURCE AVAILABILITY

Lead contact—Further information and requests for resources and reagents should be directed to the Lead Contact, Joel R. Meyerson (jrm2008@med.cornell.edu).

Materials availability—Requests for resources and reagents will be fulfilled by the Lead Contact with a completed Materials Transfer Agreement.

Data and code availability

- The cryo-EM density maps and model for GluK1-L-Glu have been deposited in the Electron Microscopy Data Bank (EMDB) and Protein Data Bank (PDB) under accession codes EMD-23542 and PDB: 7LVT and will be publicly available upon publication (HPUB status). The scRNA-seq database used in this study is available for download (https://portal.brain-map.org/atlases-and-data/rnaseq).

- This paper does not report original code.

- Any additional information required to reanalyze the data reported in this paper is available from the lead contact upon request.

EXPERIMENTAL MODEL AND SUBJECT DETAILS

HEK293S GnTI- cells—HEK293S GnTI- cells were purchased authenticated and free of mycoplasma from ATCC (CRL-3022). Cell stocks were frozen and stored in liquid nitrogen. Active cell cultures were maintained in DMEM supplemented with 10% fetal bovine serum and passaged by trypsin digestion.

HEK293T cells—HEK293T cells were purchased authenticated and free of mycoplasma from ATCC (CRL-11268). Active cell cultures were maintained in DMEM supplemented with 5% fetal bovine serum and passaged by trypsin digestion.

METHOD DETAILS

Protein expression and purification—The GluK1 expression construct was adapted from a previously reported construct in which the signal peptide on the full-length wild-type GluK1 receptor was replaced with the signal peptide from GluK2 (Duan et al., 2018). This construct, GluK1-SP^{GluK2}, retains complete receptor function but overcomes repression of plasma membrane trafficking by the GluK1 signal peptide. GluK1-SP^{GluK2} was cloned into the pEZT-BM vector (Morales-Perez et al., 2016) and fused in frame via a thrombin recognition site to mVenus and a Twin-Strep affinity tag. GluK1 receptor protein was produced using the BacMam method (Goehring et al., 2014). The expression construct was transformed into DH10Bac cells to produce bacmid, which was then transfected into Sf9 cells grown in ESF 921 media (Expression Systems). P1 and P2 virus production was monitored using fluorescence until virus harvesting. We note that this fluorescent signal comes from GFP under a p10 promoter which is a part of the pEZT-BM vector backbone, and is unrelated to the mVenus fluorescent protein fused to GluK1. HEK293S GnTI- cells (3.2 L) were grown in FreeStyle suspension media (GIBCO) at 37°C and 8% CO_2 to a density of 3×10^6 cells / mL before adding P2 virus at 10% (v/v) of the cell suspension (80 mL virus into 720 mL cells). The suspension was incubated at 37°C for 24 hours then sodium butyrate (Sigma) was added to a final concentration of 10 mM and flasks were shifted to 30°C and 8% CO_2. Cells were collected 96 hours after transduction by low-speed centrifugation (6,200 × g) for 20 min and flash-frozen at −80°C. Cell pellets were resuspended in ice-cold resuspension buffer (4 mL buffer per 1 g pellet) containing 20 mM Tris (pH 8.0), 300 mM NaCl, protease inhibitors (SigmaFast Protease Inhibitor Cocktail, Sigma), 0.5 mM EDTA, 25 μg/mL DNase and 1 mM PMSF and manually pipetted until no clumps remained. The cell suspension was lysed by sonication using a protocol of 15 s pulse-on and 45 s pulse-off for 3 min. The lysed suspension was centrifuged at low speed (7,200 × g) for 20 min to pellet cell debris. The supernatant was ultracentrifuged at 125,000 × g for 120 min to isolate membranes, and the membrane pellet was collected and flash frozen at −80°C.

The membrane pellet was thawed then homogenized in 20 mM Tris (pH 8.0), 300 mM NaCl, protease inhibitors (SigmaFast Protease Inhibitor Cocktail, Sigma), and 0.5 mM EDTA. Receptor protein was extracted by adding an equal volume of buffer containing 20

mM Tris (pH 8.0), 300 mM NaCl, 5% n-dodecyl-β-D-maltoside (DDM, Anatrace), 0.5% cholesteryl hemisuccinate (CHS, Anatrace), 0.8 μM aprotinin, 2 μg/mL leupeptin, 2 μM pepstatin, 0.5 mM EDTA and 1 mM PMSF, and the sample was agitated by nutation for 60 min at 4°C. The mixture was ultracentrifuged at $125,000 \times$ g for 50 minutes, then the supernatant was filtered through a 0.45 μm filter to remove debris, bound to a 5 mL StrepTrap column (GE) equilibrated with wash buffer (20 mM Tris, pH 8.0, 300 mM NaCl, 0.1% DDM, 0.01% CHS), washed with $10 \times$ column volume of wash buffer, and eluted in wash buffer supplemented with 10 mM desthiobiotin (IBA). The elution fractions were digested overnight with thrombin (1:200 w/w) then loaded onto a Superose 6 Increase 10/300 GL column equilibrated with gel-filtration buffer containing 20 mM Tris (pH 8.0), 300 mM NaCl, 0.05% DDM, and 0.001% CHS. Elution fractions were collected, analyzed by SDS-PAGE, and peak fractions were concentrated and used for cryo-EM experiments.

Cryo-EM sample preparation and data acquisition—Purified GluK1 receptor (3.5 mg/mL) was incubated with 1 mM L-Glutamate (Sigma). UltrAuFoil 1.2/1.3 300 mesh grids (Quantifoil) were plasma treated and rendered hydrophilic by reaction with PEG-thiol as described previously (Meyerson et al., 2014b). Vitrified samples were prepared by adding a 2.5 μL droplet of protein-ligand complex to a grid, then blotting (2 s blot time, zero blot force) and plunge-freezing in liquid ethane using a Vitrobot Mk IV (Thermo Fisher). Single particle images were collected with Leginon (Suloway et al., 2005) controlling an Arctica electron microscope (Thermo Fisher) operated at 200 kV and a nominal magnification of $36,000 \times$ and equipped with a K3 camera (Gatan) set in super-resolution mode giving a 0.5480Å pixel size. Exposures were dose-fractionation into 40 frames using a total exposure of 2.8 s and total dose of 51.0 to 52.0 e-Å^{-2}. A total of 6,643 movies were recorded.

Cryo-EM image processing and structure analysis—Movie stacks were corrected for beam-induced motion using MotionCor2 with two-fold binning as implemented in Relion 3.1 (Zheng et al., 2017; Zivanov et al., 2018) yielding dose-weighted images with an image pixel size of 1.096Å. These images were used for contrast transfer function (CTF) estimation with CTFFIND4.1 (Rohou and Grigorieff, 2015). Particles were automatically picked using a three-dimensional template, extracted with box size 416 pixels, and binned to 128 pixels. Heterogeneous refinement was performed in cryoSPARC (Punjani et al., 2017) to remove false positives from autopicking. The remaining particles we re-extracted with a box size of 320 pixels without binning. Multiple rounds of *ab initio* and heterogeneous refinement were performed with C1 symmetry. The structures supported the expectation that GluK1 has C2 symmetry, so C2 symmetry was applied in the final homogeneous and non-uniform refinement steps (indicated in Figure S1). The full-length receptor structure was composed of 321,611 particles with a global resolution of 4.6Å as measured by the Fourier Shell Correlation at the 0.143 cutoff. To improve the resolution we independently refined the ATD layer and the LBD-TMD assembly. The ATD layer was refined using local refinement in cryoSPARC to a final resolution of 3.6Å. The LBD-TMD layer was refined by subjecting the particle set from the full-length structure to signal subtraction in Relion, followed by two-dimensional classification, heterogeneous refinement, homogeneous refinement, and non-uniform refinement in cryoSPARC. This yielded an LBD-TMD structure composed of 124,324 particles with 5.5Å resolution.

Structural modeling—To model GluK1-L-Glu the ATD cryo-EM map and the LBD-TMD map were first aligned to the full-length map using UCSF Chimera (Pettersen et al., 2004). This ensured that the ATD and LBD-TMD maps were correctly positioned relative to each other and the individual ATD and LBD-TMD maps were then used for modeling. The ATD was modeled by first generating a homology model for the GluK1 ATD based on the GluK2 ATD structure (PDB: 5KUF). The homology model was refined using Phenix refine (Liebschner et al., 2019) and rebuilt using Coot (Emsley et al., 2010). Because of the modest resolution in the LBD-TMD assembly the LBD and TMD layers were built using existing structures and rigid body fitting in Chimera. Specifically, the cryo-EM density for each LBD was rigid body fitted with the crystal structure of the GluK1 LBD bound by L-Glu (PDB: 1TXF). The TMD region was built by generating a homology model of the GluK1 TMD based on the GluK2 TMD structure (PDB: 5KUF) and then fitted into the cryo-EM density. The ATD-LBD linkers, LBD-TMD linkers, M2 helices and C-terminal domains were not resolved or modeled. Molecular graphics were prepared using ChimeraX (Goddard et al., 2018) and PyMOL.

scRNA-seq analysis—scRNA sequence analysis was done using a publicly available anterior lateral motor cortex dataset (Tasic et al., 2018) and using previously described approaches (Lee et al., 2020). These approaches accounted for low false positives and under-sampling and thus imposed a threshold of five copies per million for most analysis. Data were analyzed using R Studio, Microsoft Excel, Prism and Origin.

Single molecule pulldown (SiMPull)—To generate constructs suitable for single molecule pull-down experiments we used an overall design with N-terminal signal peptide from rat mGluR5 (Lee et al., 2020), followed by affinity tags (HA or FLAG), self-labeling protein tags capable of conjugation to organic dyes (SNAP, CLIP, or Halo), and rat KAR genes (GluK1, GluK2, GluK3, or GluK5). Cloning was done in the pRK5 vector using Gibson assembly (NEBuilder HiFi kit, NEB) and yielded the constructs used for experiments: GluK1-HA/SNAP, GluK1-FLAG/CLIP, GluK1-Halo, GluK1-HA, GluK2-HA/SNAP, GluK2-SNAP, GluK2-FLAG/CLIP, GluK2-HA/Halo, GluK2-Halo, GluK3-HA/SNAP, GluK3-SNAP, GluK5-HA/Halo, GluK5-Halo, and GluK5-HA/SNAP. These constructs are presented schematically in Table S2.

SNAP-, CLIP- or Halo-tagged KARs were expressed in HEK293T cells in media containing 10% FBS at 37°C, 5% CO_2 on 18 mm poly-L-lysine-coated coverslips. A total of 2–3 μg of KAR plasmids were transfected using Lipofectamine 2000 (Thermo Scientific). At 24 hr post-transfection, cell media was changed with fresh media containing 10 mM NaButyrate and moved to 30°C, 10% CO_2 incubator. After 48 hr expression, cells were washed with Extracellular buffer (EX) containing (in mM): 10 HEPES, 135 NaCl, 5.4 KCl, 2 $CaCl_2$, 1 $MaCl_2$, pH 7.4 and labeled with 2 μM SBG-OG for HA-SNAP tagged KARs, BC-DY547 for FLAG-CLIP tagged GluKs, or CA-sulfo549 or CA-sulfo646 for HA-Halo tagged KARs in EX for 45 min at 37°C. For KAR di-heteromer conditions using SNAP- and CLIP- tagged KARs, cells were first labeled with 2 μM SBG-OregonGreen for 45 min followed by 2 μM BC-DY547 for 45 min. For three-color experiments, SNAP was first labeled with 2 μM SBG-OG for 45 min, followed by 2 μM BC-DY547 and CA-sulfo646 together for 45

min. After washing with EX solution, cells were imaged using a 60x objective (NA. 1.49) on an inverted microscope (IX83) with 488 nm, 561 nm, and 640 nm lasers used to excite OregonGreen, DY547 (or Sulfo549), and Sulfo646, respectively.

For SiMPull, labeled cells were gently harvested using 1x PBS (0 Ca^{2+}/Mg^{2+}). Cells were pelleted at $10,000 \times g$, 4°C for 1 min and lysed using 1% DDM lysis buffer containing 0.1% CHS and protease inhibitor for 1 hour at 4°C. Lysed cells were then centrifuged at 16,000 $\times g$ for 20 min at 4°C and supernatant was collected. KAR heteromers were visualized using two-color (di-heteromer conditions) or three-color (tri-heteromer or tetra-heteromer conditions) SiMPull. A microflow chamber was prepared by passivating a glass coverslip and quartz slide with mPEG-SVA and biotinylated PEG (MW = 5000, 50:1 molar ratio, Laysan Bio) as previously described (Gutzeit et al., 2019; Jain et al., 2011; Lee et al., 2020). Prior to each experiment, a microflow chamber was incubated with 0.2 mg/ml NeutrAvidin for 2 min then incubated with 0.002 mg/ml of biotinylated anti-HA antibody (ab26228, abcam) or a biotinylated anti-FLAG antibody (F9291, Sigma-Aldrich) in T50 buffer (50 mM NaCl, 10 mM Tris, pH 8.0) for 30 min. The flow chambers were rinsed with T50 buffer after each conjugation step. Fresh cell lysate containing fluorescently labeled receptors were then diluted using dilution buffer containing 0.1% DDM and 0.001% CHS in EX buffer and added to the flow chamber. When a desired single molecule spot density (~0.2 spots/μm^2) was obtained, unbound receptors were washed with the dilution buffer and imaging buffer comprising an oxygen scavenging system (1 mg/ml glucose oxidase, 0.04 mg/ml catalase, 0.8% w/v D-glucose) and photostabilizing agents (5 mM cyclo-octatetraene) was added.

Single molecule movies were recorded as described previously (Gutzeit et al., 2019; Lee et al., 2020) using a 100x objective (NA 1.49) on an inverted microscope (Olympus IX83) with total internal reflection (TIR) mode at 20 Hz with 50 ms exposure time with two sCMOS camera (Hamamatsu ORCA-Flash4v3.0). Samples were excited with 488 nm, 561 nm and 640 nm lasers to excite SBG-OG, BC-DY547 (or CA-sulfo549) and CA-sulfo646, respectively. Single molecule movies were recorded sequentially from the longest to the shortest fluorescence wavelength until > 90% molecules were bleached in the field of each movie. Single molecule movies were analyzed using a custom-built LabVIEW program (Ulbrich and Isacoff, 2007). Briefly, each movie from different channels was concatenated and loaded on the analysis program to visualize each channel for identification of co-localized molecules. Bleaching steps were assigned by inspecting the fluorescence traces manually for each molecule and plotting to show the bleaching step distribution. Data were obtained from at least two separate experimental days and averaged across multiple movies using Prism (GraphPad).

Single molecule Förster resonance energy transfer (smFRET)—smFRET experiments were performed on an inverted microscope (Olympus IX83) in TIR mode with a 100x objective (NA = 1.49) and a 561 nm laser diode. Movies were recorded simultaneously with two sCMOS ORCA-Flash4 v3.0 cameras (Hamamatsu) separated by a dichroic mirror and with appropriate emission filters for donor (595/50) and acceptor (655LP) as described previously (Acosta-Ruiz et al., 2020). Following 48 hr expression, SNAP- or CLIP-tagged GluKs were labeled for 45 min at 37°C with donor (benzylguanine [BG]-LD555 or benzylcytosine [BC]-LD555) and acceptor (BG-LD655 or BC-LD655) dyes

(Lumidyne Technologies) dissolved in EX buffer. After labeling, lysates were prepared and protein was immobilized as described for SiMPull. Single molecule fluorescence movies were recorded by exciting the donor (LD555) with 561 nm laser at 30 ms/frame in the presence of imaging buffer. smFRET data analysis was performed using SPARTAN (Juette et al., 2016). FRET histograms (averaged from at least five separate movies per condition from at least two separate experimental days) were plotted using OriginPro software.

Functional characterization of SiMPull KAR constructs in HEK293T cells—The functionality of tagged KAR constructs was verified in whole-cell patch clamp recordings. HEK293T cells were grown in DMEM with 8% FBS at 37°C and 5% CO_2 on plastic coverslips. Transfections were carried out using polyethylenimine (PEI) 25.000 with ~0.4 μg of plasmid DNA per ml medium and 0.05 μg mEGFP as transfection marker. FLAG/CLIP-GluK2 and HA/Halo-GluK5 or HA/SNAP-GluK5 were co-transfected in 1:2 ratio.

Experiments were performed 48 hr after transfection. The external solution contained 138 mM NaCl, 1.5 mM KCl, 2.5 mM $CaCl_2$, 1.2 mM $MgCl_2$ and 10 mM HEPES, pH 7.3. Desensitization was blocked by pre-incubation with 0.3 mg/ml concanavalin A (ConA, Sigma #L7647). Patch pipettes (4–8 MΩ resistance, borosilicate glass) were filled with internal solution containing 135 mM K-gluconate, 10 mM NaCl, 2 mM $MgCl_2$, 1 mM EGTA, 10 mM HEPES, pH 7.4. Whole-cell recordings were performed using a Patchstar micro-manipulator (Scientifica), an Axopatch 200B patch-clamp amplifier with a Digidata 1550 A/D converter and pClamp 10.7 software (all Molecular Devices) on a DMi8 inverse microscope (Leica). Recordings were performed in voltage-clamp mode ($U_h = -70$ mV) at 22–25°C. External solution and agonists (1 mM L-glutamate, Sigma #49449 and 300 μM (S)-5-iodowillardiine (5-IW), Abcam #ab120222) were applied by means of a gravity-driven bath perfusion (~5 ml/min). For the evaluation of peak and steady-state currents only recordings with ligand-induced currents > 20 pA were taken into account.

QUANTIFICATION AND STATISTICAL ANALYSIS

scRNA-seq data were analyzed using R Studio, Microsoft Excel, and GraphPad Prism and Origin Pro was used for generating violin plots, co-expression heatmaps, scatterplots and bar graphs. Statistical details of experiments can be found in the results, legends, and STAR methods. SiMPull data were analyzed using ImageJ, LabVIEW, Microsoft Excel and plotted using GraphPad Prism. smFRET data were analyzed using SPARTAN (Juette et al., 2016) and plotted using Origin Pro. Statistical details of experiments can be found in the results, legends, and STAR methods. Whole cell patch clamp recording data were analyzed using pClamp 10.7 software and plotted using Excel. Statistical details of experiments can be found in the legends.

Supplementary Material

Refer to Web version on PubMed Central for supplementary material.

ACKNOWLEDGMENTS

REFERENCES

Acosta-Ruiz A, Gutzeit VA, Skelly MJ, Meadows S, Lee J, Parekh P, Orr AG, Liston C, Pleil KE, Broichhagen J, and Levitz J (2020). Branched Photoswitchable Tethered Ligands Enable Ultra-efficient Optical Control and Detection of G Protein-Coupled Receptors In Vivo. Neuron 105, 446–463.e13. [PubMed: 31784287]

Ayalon G, and Stern-Bach Y (2001). Functional assembly of AMPA and kainate receptors is mediated by several discrete protein-protein interactions. Neuron 31, 103–113. [PubMed: 11498054]

Bahn S, Volk B, and Wisden W (1994). Kainate receptor gene expression in the developing rat brain. J. Neurosci 14, 5525–5547. [PubMed: 8083752]

Birke R, Ast J, Roosen DA, Mathes B, Roßmann K, Huhn C, Jones B, Lehmann M, Haucke V, Hodson DJ, et al. (2021). Sulfonated rhodamines as impermeable labelling substrates for cell surface protein visualization. bioRxiv. 10.1101/2021.03.16.435698.

Contractor A, Mulle C, and Swanson GT (2011). Kainate receptors coming of age: milestones of two decades of research. Trends Neurosci. 34, 154–163. [PubMed: 21256604]

Copits BA, and Swanson GT (2012). Dancing partners at the synapse: auxiliary subunits that shape kainate receptor function. Nat. Rev. Neurosci 13, 675–686. [PubMed: 22948074]

Cui C, and Mayer ML (1999). Heteromeric kainate receptors formed by the coassembly of GluR5, GluR6, and GluR7. J. Neurosci 19, 8281–8291. [PubMed: 10493729]

Duan GF, Ye Y, Xu S, Tao W, Zhao S, Jin T, Nicoll RA, Shi YS, and Sheng N (2018). Signal peptide represses GluK1 surface and synaptic trafficking through binding to amino-terminal domain. Nat. Commun 9, 4879. [PubMed: 30451858]

Emsley P, Lohkamp B, Scott WG, and Cowtan K (2010). Features and development of Coot. Acta Crystallogr. D Biol. Crystallogr 66, 486–501. [PubMed: 20383002]

Garcia EP, Mehta S, Blair LAC, Wells DG, Shang J, Fukushima T, Fallon JR, Garner CC, and Marshall J (1998). SAP90 binds and clusters kainate receptors causing incomplete desensitization. Neuron 21, 727–739. [PubMed: 9808460]

Goddard TD, Huang CC, Meng EC, Pettersen EF, Couch GS, Morris JH, and Ferrin TE (2018). UCSF ChimeraX: Meeting modern challenges in visualization and analysis. Protein Sci. 27, 14–25. [PubMed: 28710774]

Goehring A, Lee CH, Wang KH, Michel JC, Claxton DP, Baconguis I, Althoff T, Fischer S, Garcia KC, and Gouaux E (2014). Screening and large-scale expression of membrane proteins in mammalian cells for structural studies. Nat. Protoc 9, 2574–2585. [PubMed: 25299155]

Göngrich C, Krapacher FA, Munguba H, Fernández-Suárez D, Andersson A, Hjerling-Leffler J, and Ibáñez CF (2020). ALK4 coordinates extracellular and intrinsic signals to regulate development of cortical somatostatin interneurons. J. Cell Biol 219, e2019.

Gutzeit VA, Thibado J, Stor DS, Zhou Z, Blanchard SC, Andersen OS, and Levitz J (2019). Conformational dynamics between transmembrane domains and allosteric modulation of a metabotropic glutamate receptor. eLife 8, e45116. [PubMed: 31172948]

Hadzic M, Jack A, and Wahle P (2017). Ionotropic glutamate receptors: Which ones, when, and where in the mammalian neocortex. J. Comp. Neurol 525, 976–1033. [PubMed: 27560295]

Heckmann M, Bufler J, Franke C, and Dudel J (1996). Kinetics of homomeric GluR6 glutamate receptor channels. Biophys. J 71, 1743–1750. [PubMed: 8889151]

Herb A, Burnashev N, Werner P, Sakmann B, Wisden W, and Seeburg PH (1992). The KA-2 subunit of excitatory amino acid receptors shows wide-spread expression in brain and forms ion channels with distantly related subunits. Neuron 8, 775–785. [PubMed: 1373632]

Herbrechter R, Hube N, Buchholz R, and Reiner A (2021). Splicing and editing of ionotropic glutamate receptors: a comprehensive analysis based on human RNA-Seq data. Cell. Mol. Life Sci 78, 5605–5630. [PubMed: 34100982]

Hilscher MM, Leão RN, Edwards SJ, Leão KE, and Kullander K (2017). Chrna2-Martinotti Cells Synchronize Layer 5 Type A Pyramidal Cells via Rebound Excitation. PLoS Biol. 15, e2001392. [PubMed: 28182735]

Hollmann M, and Heinemann S (1994). Cloned glutamate receptors. Annu. Rev. Neurosci 17, 31–108. [PubMed: 8210177]

Jain A, Liu R, Ramani B, Arauz E, Ishitsuka Y, Ragunathan K, Park J, Chen J, Xiang YK, and Ha T (2011). Probing cellular protein complexes using single-molecule pull-down. Nature 473, 484–488. [PubMed: 21614075]

Juette MF, Terry DS, Wasserman MR, Altman RB, Zhou Z, Zhao H, and Blanchard SC (2016). Single-molecule imaging of non-equilibrium molecular ensembles on the millisecond timescale. Nat. Methods 13, 341–344. [PubMed: 26878382]

Khanra N, Brown PMGE, Perozzo AM, Bowie D, and Meyerson JR (2021). Architecture and structural dynamics of the heteromeric GluK2/K5 kainate receptor. eLife 10, e66097. [PubMed: 33724189]

Kumar J, and Mayer ML (2010). Crystal structures of the glutamate receptor ion channel GluK3 and GluK5 amino-terminal domains. J. Mol. Biol 404, 680–696. [PubMed: 20951142]

Kumar J, Schuck P, and Mayer ML (2011). Structure and assembly mechanism for heteromeric kainate receptors. Neuron 71, 319–331. [PubMed: 21791290]

Kumari J, Vinnakota R, and Kumar J (2019). Structural and Functional Insights into GluK3-kainate Receptor Desensitization and Recovery. Sci. Rep 9, 10254. [PubMed: 31311973]

Lee J, Munguba H, Gutzeit VA, Singh DR, Kristt M, Dittman JS, and Levitz J (2020). Defining the Homo- and Heterodimerization Propensities of Metabotropic Glutamate Receptors. Cell Rep. 31, 107605. [PubMed: 32375054]

Lerma J, and Marques JM (2013). Kainate receptors in health and disease. Neuron 80, 292–311. [PubMed: 24139035]

Lerner E, Barth A, Hendrix J, Ambrose B, Birkedal V, Blanchard SC, Börner R, Sung Chung H, Cordes T, Craggs TD, et al. (2021). FRET-based dynamic structural biology: Challenges, perspectives and an appeal for open-science practices. eLife 10, e60416. [PubMed: 33779550]

Levitz J, Royal P, Comoglio Y, Wdziekonski B, Schaub S, Clemens DM, Isacoff EY, and Sandoz G (2016). Heterodimerization within the TREK channel subfamily produces a diverse family of highly regulated potassium channels. Proc. Natl. Acad. Sci. USA 113, 4194–4199. [PubMed: 27035963]

Liebschner D, Afonine PV, Baker ML, Bunkóczi G, Chen VB, Croll TI, Hintze B, Hung LW, Jain S, McCoy AJ, et al. (2019). Macromolecular structure determination using X-rays, neutrons and electrons: recent developments in Phenix. Acta Crystallogr. D Struct. Biol 75, 861–877. [PubMed: 31588918]

Litwin DB, Paudyal N, Carrillo E, Berka V, and Jayaraman V (2020). The structural arrangement and dynamics of the heteromeric GluK2/GluK5 kainate receptor as determined by smFRET. Biochim. Biophys. Acta Biomembr 1862, 183001. [PubMed: 31194959]

Ma Y, Hu H, Berrebi AS, Mathers PH, and Agmon A (2006). Distinct subtypes of somatostatin-containing neocortical interneurons revealed in transgenic mice. J. Neurosci 26, 5069–5082. [PubMed: 16687498]

Maraschi A, Ciammola A, Folci A, Sassone F, Ronzitti G, Cappelletti G, Silani V, Sato S, Hattori N, Mazzanti M, et al. (2014). Parkin regulates kainate receptors by interacting with the GluK2 subunit. Nat. Commun 5, 5182. [PubMed: 25316086]

Matsuda K, Budisantoso T, Mitakidis N, Sugaya Y, Miura E, Kakegawa W, Yamasaki M, Konno K, Uchigashima M, Abe M, et al. (2016). Trans-synaptic Modulation of Kainate Receptor Functions by C1q-like Proteins. Neuron 90, 752–767. [PubMed: 27133466]

Meyerson JR, Kumar J, Chittori S, Rao P, Pierson J, Bartesaghi A, Mayer ML, and Subramaniam S (2014a). Structural mechanism of glutamate receptor activation and desensitization. Nature 514, 328–334. [PubMed: 25119039]

Meyerson JR, Rao P, Kumar J, Chittori S, Banerjee S, Pierson J, Mayer ML, and Subramaniam S (2014b). Self-assembled monolayers improve protein distribution on holey carbon cryo-EM supports. Sci. Rep 4, 7084. [PubMed: 25403871]

Meyerson JR, Chittori S, Merk A, Rao P, Han TH, Serpe M, Mayer ML, and Subramaniam S (2016). Structural basis of kainate subtype glutamate receptor desensitization. Nature 537, 567–571. [PubMed: 27580033]

Morales-Perez CL, Noviello CM, and Hibbs RE (2016). Manipulation of Subunit Stoichiometry in Heteromeric Membrane Proteins. Structure 24, 797–805. [PubMed: 27041595]

Mulle C, Sailer A, Swanson GT, Brana C, O'Gorman S, Bettler B, and Heinemann SF (2000). Subunit composition of kainate receptors in hippocampal interneurons. Neuron 28, 475–484. [PubMed: 11144357]

Muñoz W, Tremblay R, Levenstein D, and Rudy B (2017). Layer-specific modulation of neocortical dendritic inhibition during active wakefulness. Science 355, 954–959. [PubMed: 28254942]

Naka A, Veit J, Shababo B, Chance RK, Risso D, Stafford D, Snyder B, Egladyous A, Chu D, Sridharan S, et al. (2019). Complementary networks of cortical somatostatin interneurons enforce layer specific control. eLife 8, e43696. [PubMed: 30883329]

Nasu-Nishimura Y, Hurtado D, Braud S, Tang TTT, Isaac JTR, and Roche KW (2006). Identification of an endoplasmic reticulum-retention motif in an intracellular loop of the kainate receptor subunit KA2. J. Neurosci 26, 7014–7021. [PubMed: 16807331]

Paoletti P, Bellone C, and Zhou Q (2013). NMDA receptor subunit diversity: impact on receptor properties, synaptic plasticity and disease. Nat. Rev. Neurosci 14, 383–400. [PubMed: 23686171]

Paternain AV, Herrera MT, Nieto MA, and Lerma J (2000). GluR5 and GluR6 kainate receptor subunits coexist in hippocampal neurons and coassemble to form functional receptors. J. Neurosci 20, 196–205. [PubMed: 10627597]

Petralia RS, Wang Y-X, and Wenthold RJ (1994). Histological and ultra-structural localization of the kainate receptor subunits, KA2 and GluR6/7, in the rat nervous system using selective antipeptide antibodies. J. Comp. Neurol 349, 85–110. [PubMed: 7852627]

Pettersen EF, Goddard TD, Huang CC, Couch GS, Greenblatt DM, Meng EC, and Ferrin TE (2004). UCSF Chimera–a visualization system for exploratory research and analysis. J. Comput. Chem 25, 1605–1612. [PubMed: 15264254]

Pinheiro PS, Perrais D, Coussen F, Barhanin J, Bettler B, Mann JR, Malva JO, Heinemann SF, and Mulle C (2007). GluR7 is an essential subunit of presynaptic kainate autoreceptors at hippocampal mossy fiber synapses. Proc. Natl. Acad. Sci. USA 104, 12181–12186. [PubMed: 17620617]

Poc P, Gutzeit VA, Ast J, Lee J, Jones BJ, D'Este E, Mathes B, Lehmann M, Hodson DJ, Levitz J, and Broichhagen J (2020). Interrogating surface *versus* intracellular transmembrane receptor populations using cell-impermeable SNAP-tag substrates. Chem. Sci. (Camb.) 11, 7871–7883.

Pollok S, and Reiner A (2020). Subunit-selective iGluR antagonists can potentiate heteromeric receptor responses by blocking desensitization. Proc. Natl. Acad. Sci. USA 117, 25851–25858. [PubMed: 32999066]

Poulin JF, Tasic B, Hjerling-Leffler J, Trimarchi JM, and Awatramani R (2016). Disentangling neural cell diversity using single-cell transcriptomics. Nat. Neurosci 19, 1131–1141. [PubMed: 27571192]

Punjani A, Rubinstein JL, Fleet DJ, and Brubaker MA (2017). cryo-SPARC: algorithms for rapid unsupervised cryo-EM structure determination. Nat. Methods 14, 290–296. [PubMed: 28165473]

Reiner A, and Levitz J (2018). Glutamatergic Signaling in the Central Nervous System: Ionotropic and Metabotropic Receptors in Concert. Neuron 98, 1080–1098. [PubMed: 29953871]

Reiner A, Arant RJ, and Isacoff EY (2012). Assembly stoichiometry of the GluK2/GluK5 kainate receptor complex. Cell Rep. 1, 234–240. [PubMed: 22509486]

Ren Z, Riley NJ, Garcia EP, Sanders JM, Swanson GT, and Marshall J (2003). Multiple trafficking signals regulate kainate receptor KA2 subunit surface expression. J. Neurosci 23, 6608–6616. [PubMed: 12878702]

Rohou A, and Grigorieff N (2015). CTFFIND4: Fast and accurate defocus estimation from electron micrographs. J. Struct. Biol 192, 216–221. [PubMed: 26278980]

Roy R, Hohng S, and Ha T (2008). A practical guide to single-molecule FRET. Nat. Methods 5, 507–516. [PubMed: 18511918]

Royal P, Andres-Bilbe A,Ávalos Prado P, Verkest C, Wdziekonski B, Schaub S, Baron A, Lesage F, Gasull X, Levitz J, and Sandoz G (2019). Migraine-Associated TRESK Mutations Increase Neuronal Excitability through Alternative Translation Initiation and Inhibition of TREK. Neuron 101, 232–245.e6. [PubMed: 30573346]

Schiffer HH, Swanson GT, and Heinemann SF (1997). Rat GluR7 and a carboxy-terminal splice variant, GluR7b, are functional kainate receptor subunits with a low sensitivity to glutamate. Neuron 19, 1141–1146. [PubMed: 9390526]

Straub C, Noam Y, Nomura T, Yamasaki M, Yan D, Fernandes HB, Zhang P, Howe JR, Watanabe M, Contractor A, and Tomita S (2016). Distinct Subunit Domains Govern Synaptic Stability and Specificity of the Kainate Receptor. Cell Rep. 16, 531–544. [PubMed: 27346345]

Suloway C, Pulokas J, Fellmann D, Cheng A, Guerra F, Quispe J, Stagg S, Potter CS, and Carragher B (2005). Automated molecular microscopy: the new Leginon system. J. Struct. Biol 151, 41–60. [PubMed: 15890530]

Tasic B, Yao Z, Graybuck LT, Smith KA, Nguyen TN, Bertagnolli D, Goldy J, Garren E, Economo MN, Viswanathan S, et al. (2018). Shared and distinct transcriptomic cell types across neocortical areas. Nature 563, 72–78. [PubMed: 30382198]

Thibado JK, Tano JY, Lee J, Salas-Estrada L, Provasi D, Strauss A, Marcelo Lamim Ribeiro J, Xiang G, Broichhagen J, Filizola M, et al. (2021). Differences in interactions between transmembrane domains tune the activation of metabotropic glutamate receptors. eLife 10, e67027. [PubMed: 33880992]

Tomita S, and Castillo PE (2012). Neto1 and Neto2: auxiliary subunits that determine key properties of native kainate receptors. J. Physiol 590, 2217–2223. [PubMed: 22431337]

Ulbrich MH, and Isacoff EY (2007). Subunit counting in membrane-bound proteins. Nat. Methods 4, 319–321. [PubMed: 17369835]

Veran J, Kumar J, Pinheiro PS, Athané A, Mayer ML, Perrais D, and Mulle C (2012). Zinc potentiates GluK3 glutamate receptor function by stabilizing the ligand binding domain dimer interface. Neuron 76, 565–578. [PubMed: 23141068]

Vernon CG, Copits BA, Stolz JR, Guzmán YF, and Swanson GT (2017). N-glycan content modulates kainate receptor functional properties. J. Physiol 595, 5913–5930. [PubMed: 28714086]

Wang LY, Taverna FA, Huang XP, MacDonald JF, and Hampson DR (1993). Phosphorylation and modulation of a kainate receptor (GluR6) by cAMP-dependent protein kinase. Science 259, 1173–1175. [PubMed: 8382377]

Werner P, Voigt M, Keinänen K, Wisden W, and Seeburg PH (1991). Cloning of a putative high-affinity kainate receptor expressed predominantly in hippocampal CA3 cells. Nature 351, 742–744. [PubMed: 1648176]

Wisden W, and Seeburg PH (1993). A complex mosaic of high-affinity kainate receptors in rat brain. J. Neurosci 13, 3582–3598. [PubMed: 8393486]

Wyeth MS, Pelkey KA, Yuan X, Vargish G, Johnston AD, Hunt S, Fang C, Abebe D, Mahadevan V, Fisahn A, et al. (2017). Neto Auxiliary Subunits Regulate Interneuron Somatodendritic and Presynaptic Kainate Receptors to Control Network Inhibition. Cell Rep. 20, 2156–2168. [PubMed: 28854365]

Zhao H, Lomash S, Chittori S, Glasser C, Mayer ML, and Schuck P (2017). Preferential assembly of heteromeric kainate and AMPA receptor amino terminal domains. eLife 6, e32056. [PubMed: 29058671]

Zhao Y, Chen S, Swensen AC, Qian WJ, and Gouaux E (2019). Architecture and subunit arrangement of native AMPA receptors elucidated by cryo-EM. Science 364, 355–362. [PubMed: 30975770]

Zheng SQ, Palovcak E, Armache JP, Verba KA, Cheng Y, and Agard DA (2017). MotionCor2: anisotropic correction of beam-induced motion for improved cryo-electron microscopy. Nat. Methods 14, 331–332. [PubMed: 28250466]

Zivanov J, Nakane T, Forsberg BO, Kimanius D, Hagen WJH, Lindahl E, and Scheres SHW (2018). New tools for automated high-resolution cryo-EM structure determination in RELION-3. eLife 7, e42166. [PubMed: 30412051]

Highlights

- The cryo-EM structure of the GluK1 homomer

- Complex co-expression patterns of two or more KAR subunit types across cell types

- KAR di-heteromers can assemble with 3:1, 2:2, and 1:3 stoichiometries

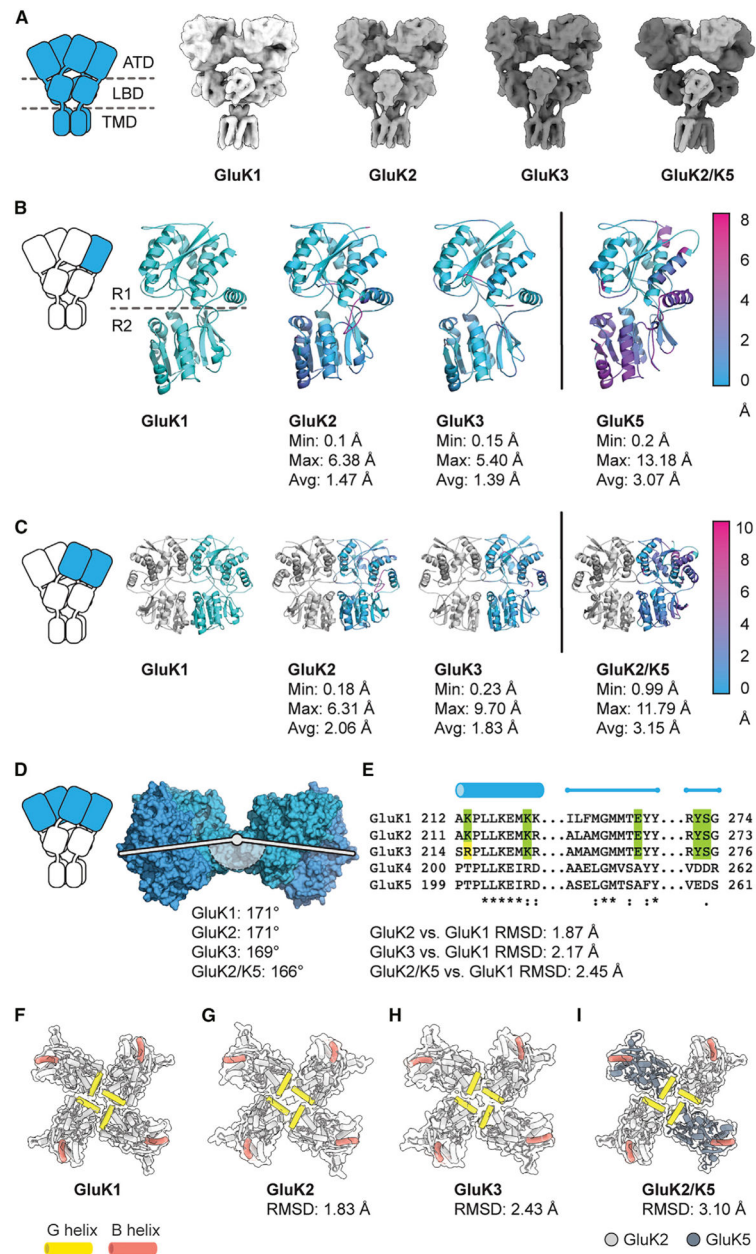- KARs can assemble as tri-heteromers and tetra-heteromers

Figure 1. Structural similarity between kainate receptors

(A) Surface view of agonist-bound GluK1, GluK2, GluK3, and GluK2/K5 structures.

(B) Comparison of KAR ATD monomers. Monomers from GluK2, GluK3, and GluK5 were aligned to GluK1 ATD monomer using R1 domains. ATDs colored according to RMSD relative to GluK1. Color maps range from 0 to 8Å RMSD.

(C) Comparison of KAR ATD dimer conformations. ATD dimers from GluK1, GluK2, and GluK3 were aligned to the GluK1 ATD dimer. Alignment made between one subunit within each ATD dimer. Subunits used for alignment colored gray and cyan/magenta for RMSD calculations. GluK2/K5 ATD dimer was aligned to the GluK1 dimer using the GluK2 subunit (gray), and GluK5 was used for RMSD calculation (cyan/magenta). The RMSD

values convey conformational differences within the ATD dimer, between GluK1 and the other KARs shown. The color map ranges from 0 to 10Å RMSD.

(D) Angle formed by KAR ATD dimers at the dimer-dimer interface. GluK1 is used in the panel, but each angle measurement was done on its corresponding KAR structure.

(E) Sequence alignment for the five KAR subunits highlighting residues involved in forming the ATD dimer-dimer interface analyzed in (D). Green indicates sequence conservation, and yellow indicates charge conservation.

(F–I) LBD layers for agonist-bound GluK1 (F), GluK2 (G), GluK3 (H), and GluK2/K5 (I) with helices B (red) and G (yellow) highlighted. PDB codes used in this figure are PDB: 5KUF (GluK2-SYM), 6JFY (GluK3-SYM), and 7KS3 (GluK2/K5-L-Glu).
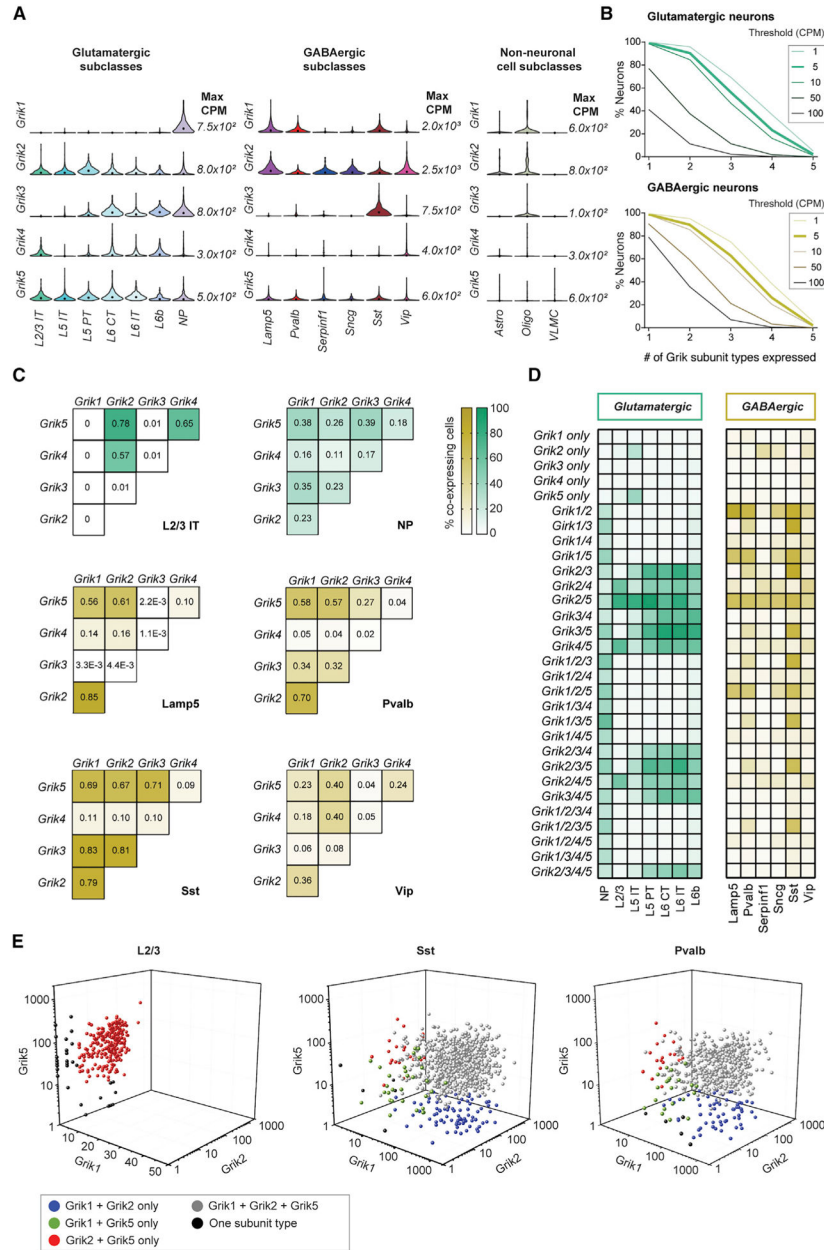
See also Figures S1 and S2.

Figure 2. scRNA-seq analysis of KAR subunit expression in mouse frontal cortex

(A) Violin plots showing relative expression of each *Grik* subunit type across glutamatergic neuron, GABAergic neuron, and non-neuronal subclasses. Different widths in each plot represent probability density (relative number of cells expressing at that range). Black dots represent the median value for each subclass. Scales represent maximum copies per million (CPMs) for each gene.

(B) Survival plots with the number of *Grik* subunit types expressed per cell for different thresholds.

(C) Paired co-expression analysis (cutoff minimum of 5 CPM) shown as heatmaps. Color range is the proportion of cells co-expressing the indicated pairs of *Grik* subunits.

(D) Co-expression analysis (cutoff minimum of 5 CPM) shown as heatmaps. Color range represents proportion of cells within that subclass expressing each *Grik* combination.
(E) 3D plots showing expression levels of *Grik1*, *Grik2*, and *Grik5* in L2/3 (left), Sst (middle), and Pvalb (right) neurons. Each point represents an individual cell and axis values are CPMs.
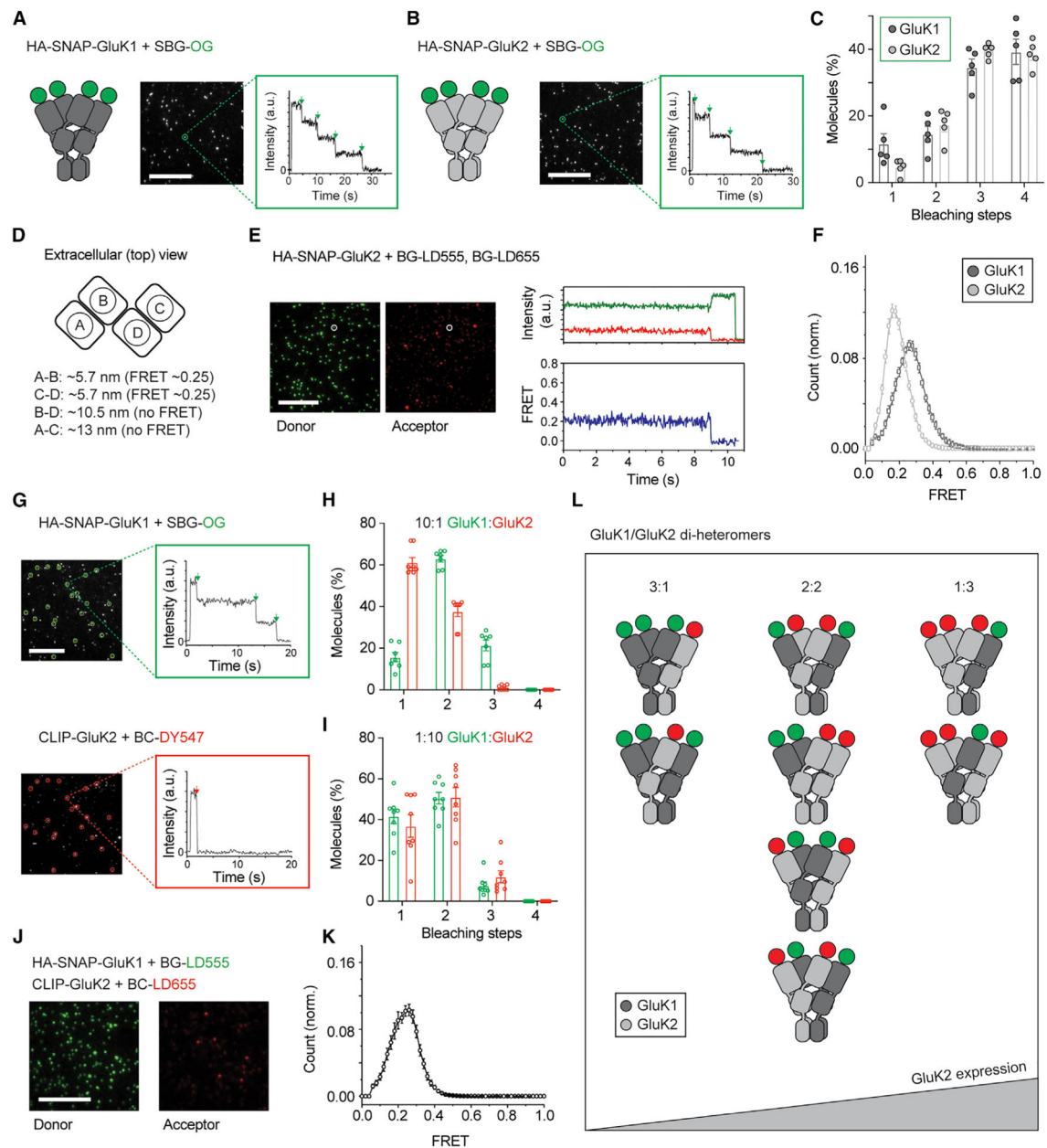See also Figure S3.

Figure 3. GluK1/K2 di-heteromers can form all possible stoichiometries in an expression-dependent manner

(A and B) Representative SiMPull images and bleaching step (green arrows) traces for HA-SNAP-GluK1 (A) and HA-SNAP-GluK2 (B) labeled with SBG-OG.

(C) Proportion of molecules with 1 to 4 bleaching steps (n = 403 and 615 molecules from 5 movies for GluK1 and GluK2, respectively).

(D) Schematic of ATD layer. Distance measurements indicate that only ATD dimers (A-B or C-D pairs) can generate FRET signals from N-terminal fluorescent tags (Förster radius, ~6 nm).

(E) Representative images (left) and traces (right) showing smFRET analysis of HA-SNAP-GluK2 homo-tetramers. Acceptor (red) bleaching followed by donor (green) recovery

confirms FRET. Single bleaching steps in each channel confirm measurements restricted to molecules with one donor and one acceptor molecule.

(F) Histograms showing smFRET values for HA-SNAP-GluK1 (n = 265 molecules; 9 movies) and HA-SNAP-GluK2 (n = 1123 molecules; 16 movies).

(G) Representative two-color SiMPull images with co-localized spots indicating GluK1/K2 di-heteromers (circled). Traces show bleaching steps in both colors for the same molecule.

(H and I) Photobleaching step distributions for HA-SNAP-GluK1 and FLAG-CLIP-GluK2 at 10:1 (H) and 1:10 (I) expression ratios (n = 416 and 406 molecules from 7 movies in H, and 185 and 220 molecules from 8 movies in I, for GluK1 and GluK2, respectively).

(J and K) Representative image (J) and histogram (K; n = 235 molecules; 15 movies) showing smFRET between HA-SNAP-GluK1 and FLAG-CLIP-GluK2, indicating ATD heterodimers formed.

(L) GluK1/K2 complexes suggested by the experiments.

Data are represented as mean ± SEM. Each point in the bar graphs represents an individual movie combined from two separate days. Scale bars are 10 μm.
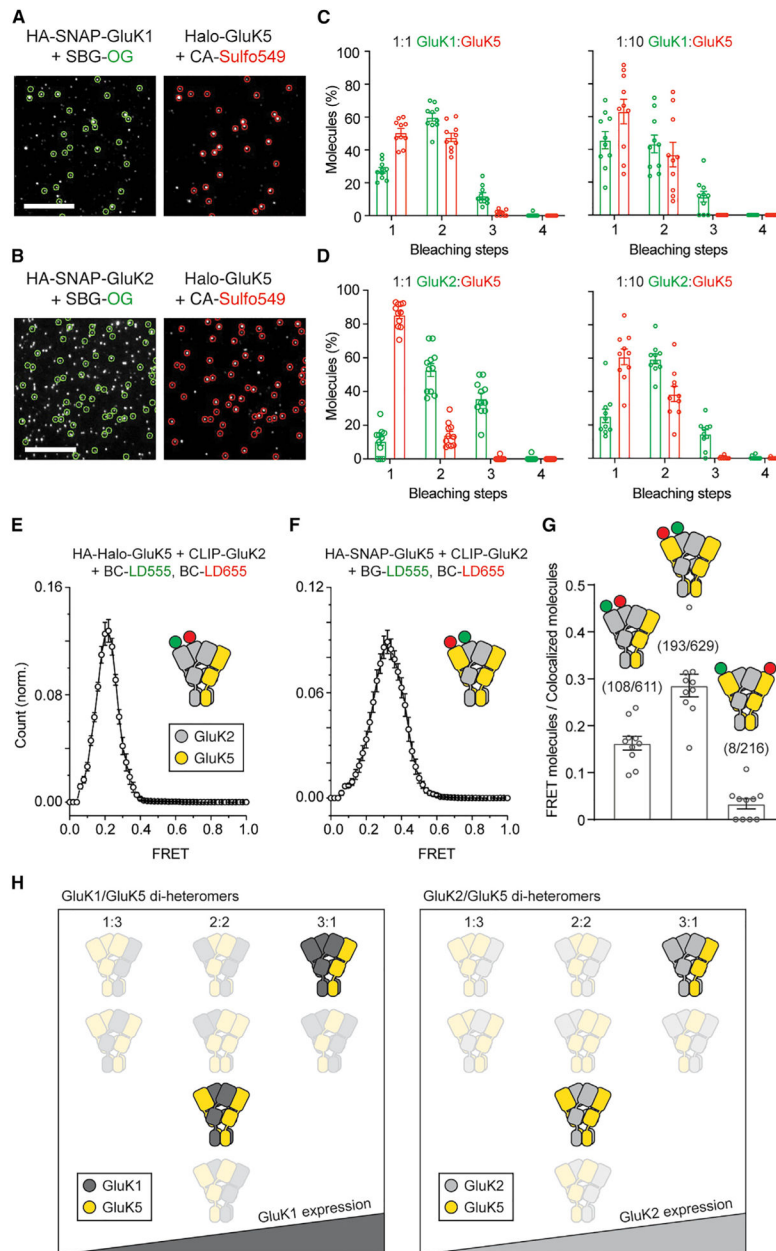
See also Figure S4.

Figure 4. GluK1/K5 and GluK2/K5 di-heteromers can incorporate one or two GluK5 subunits
(A and B) Representative images from two-color SiMPull with co-localized spots for
GluK1/K5 (A) and GluK2/K5 (B) heteromers.

(C and D) Distribution of bleaching steps for co-localized spots at two DNA transfection
ratios, indicating that up to three GluK1 (C) or GluK2 (D) subunits and up to two GluK5
subunits can exist within a heteromer. For (C), n = 305 and 494 molecules from 10 movies
at 1:1 ratio, and 124 and 203 molecules from 10 movies at 1:10 ratio, for GluK1 and GluK5,
respectively. For (D), n = 134 and 252 molecules from 10 movies at 1:1 ratio, and 448 and
991 molecules from 10 movies at 1:10 ratio, for GluK2 and GluK5, respectively

(E and F) smFRET histograms showing efficient energy transfer within GluK2 ATD homodimers (E; n = 257 molecules; 10 movies) and GluK2/K5 ATD heterodimers (F; n = 331 molecules; 11 movies).

(G) Proportion of co-localized spots (i.e., heteromers) showing FRET. FRET signal indicates ATD dimerization between labeled subunits and shows GluK2 ATD homodimers and GluK2/K5 ATD heterodimers form, but GluK5 ATD homodimers do not readily form. DNA transfection ratios are 1:10 (HA-Halo-GluK5:CLIP-GluK2) and 5:1 (HA-SNAP-GluK5:CLIP-GluK2).

(H) Possible GluK1/K5 and GluK2/K5 di-heteromers.

Data are represented as mean ± SEM. Each point in the bar graphs represents an individual movie combined from two separate days. Scale bars are 10 μm.
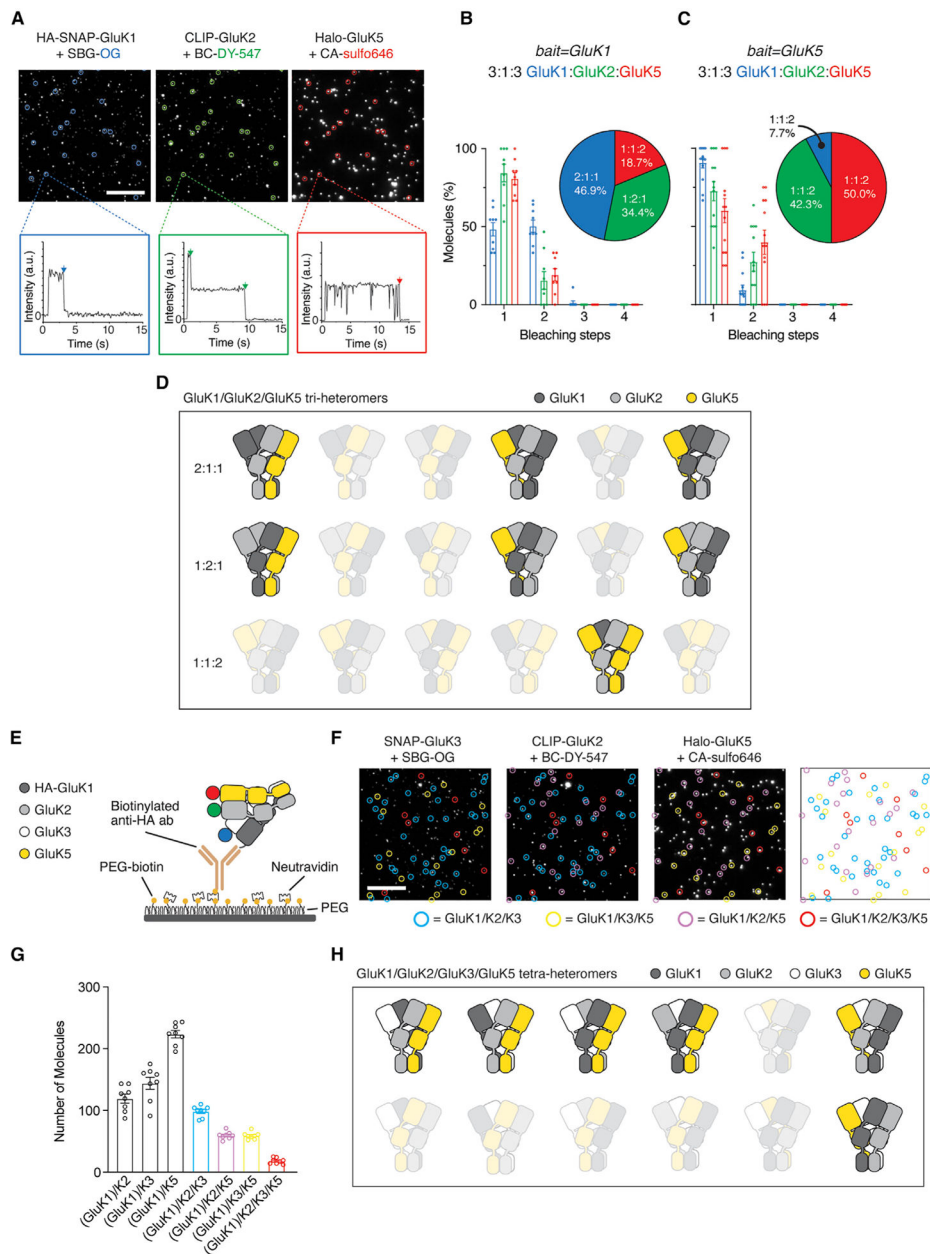
See also Figure S5.

Figure 5. Visualization of tri-heteromeric and tetra-heteromeric KARs

(A) Representative images and photobleaching traces for three-color SiMPull experiments with HA-SNAP-GluK1 as bait.

(B and C) Photobleaching step distributions for each KAR subunit in triple-colocalized spots when HA-SNAP-GluK1 (B) or HA-Halo-GluK5 (C) used as bait. Pie charts show the distribution of stoichiometries when analysis restricted to triple-colocalized spots which show four bleaching steps. For (B), n = 89, 123, and 117 molecules from 9 movies for GluK1,GluK2, and GluK5, respectively. For (C), n = 107, 130, and 98 molecules from 13 movies for GluK1,GluK2, and GluK5, respectively.

(D) Possible GluK1/K2/K5 tri-heteromers.

(E) Schematic of SiMPull using three fluorescently tagged subunits (SNAP-GluK3, FLAG-CLIP-GluK2, Halo-GluK5) and pull-down via HA-GluK1.

(F) Representative image with three colors. Double- and triple-co-localized spots circled in different colors. Panel on right shows superposition of the locations of all co-localized molecules.

(G) Relative proportion of spots containing combinations of at least 2, 3, or 4 KAR subunits. Double-co-localized spots either represent tri-heteromers or tetra-heteromers. Triple-co-localized spots (red bar) represent tetra-heteromers. All spots inferred to have a GluK1 subunit because it is the bait for pull-down.

(H) Possible GluK1/K2/K3/K5 tetra-heteromers.

Data are represented as mean ± SEM. Each point in the bar graphs represents an individual movie combined from two separate days. Scale bars are 10 μm.

See also Figure S6.

KEY RESOURCES TABLE

REAGENT or RESOURCE	SOURCE	IDENTIFIER
Antibodies		
Anti-HA tag antibody (Biotinylated)	abcam	Cat#ab6438; RRID:AB_2115899
Anti-FLAG tag antibody (Biotinylated)	Sigma-Aldrich	Cat#F9291; RRID:AB_439698
Chemicals, peptides, and recombinant proteins		
DDM/CHS mix	Anatrace	Cat#D310-CH210
FreeStyle suspension media	GIBCO	Cat#12338-026
DMEM	GIBCO	Cat#11-995-081
Fetal bovine serum	GIBCO	Cat#16140071
NeutrAvidin protein	Thermo Fisher Scientific	Cat#31000
benzylguanine (BG)-LD555	Gutzeit et al., 2019	N/A
benzylguanine (BG)-LD655	Gutzeit et al., 2019	N/A
benzylcytosine (BC)-LD555	This paper	N/A
benzylcytosine (BC)-LD655	This paper	N/A
CLIP-Surface 547 (DY547)	New England Biolabs	Cat#S9233S
SBG-OregonGreen	Poc et al., 2020	N/A
CA-Sulfo549	This paper	N/A
CA-Sulfo646	This paper	N/A
mPEG	Laysan Bio	Cat#BIO-PEG-SVA-5K, MPEG-SVA-5K
biotinylated mPEG	Laysan Bio	Cat#BIO- PEG-SVA-5K, MPEG-SVA-5K
DMEM	Thermo Fisher Scientific	Cat#11995073
Fetal bovine serum	Thermo Fisher Scientific	Cat#10437028
Lipofectamine 2000	Thermo Fisher Scientific	Cat#11668-019
Poly-L-lysine hydrobromide	Sigma-Aldrich	Cat#P2636
Polyethylenimine, branched 25.000	Sigma-Aldrich	Cat#408727
Concanavalin A from *Canavalia ensiformis*	Sigma-Aldrich	Cat#L7647
(S)-5-Iodowillardiine	Abcam	Cat#ab120222
L-Glutamic acid	Sigma-Aldrich	Cat#L49449
DMEM, high glucose	Sigma-Aldrich	Cat#D6429
Fetal bovine serum (FBS)	Sigma-Aldrich	Cat#F9665
Deposited data		
Coordinates of the GluK1 receptor in complex with L-Glu	This paper	PDB: 7LVT
Cryo-EM map of the GluK1 receptor in complex with L-Glu	This paper	EMDB: EMD-23542
Experimental models: Cell lines		
HEK293S GnTI-	ATCC	CRL-3022
HEK293T	ATCC	CRL-11268
Recombinant DNA		
pEZT-BM vector	Morales-Perez et al., 2016	Addgene Plasmid #74099
GluK1-HA/SNAP in pRK5	This paper	N/A
GluK1-FLAG/CLIP in pRK5	This paper	N/A

REAGENT or RESOURCE	SOURCE	IDENTIFIER
GluK1-Halo in pRK5	This paper	N/A
GluK1-HA in pRK5	This paper	N/A
GluK2-HA/SNAP in pRK5	This paper	N/A
GluK2-SNAP in pRK5	This paper	N/A
GluK2-FLAG/CLIP in pRK5	This paper	N/A
GluK2-HA/Halo in pRK5	This paper	N/A
GluK2-Halo in pRK5	This paper	N/A
GluK3-HA/SNAP in pRK5	This paper	N/A
GluK3-SNAP in pRK5	This paper	N/A
GluK5-HA/Halo in pRK5	This paper	N/A
GluK5-Halo in pRK5	This paper	N/A
GluK5-HA/SNAP in pRK5	This paper	N/A
Software and algorithms		
Relion 3.1	Zivanov et al., 2018	https://www3.mrc-lmb.cam.ac.uk/relion/index.php/Main_Page
cryoSPARC	Punjani et al., 2017	https://cryosparc.com/
UCSF Chimera	Pettersen et al., 2004	https://www.cgl.ucsf.edu/chimera/
UCSF ChimeraX	Goddard et al., 2018	https://www.cgl.ucsf.edu/chimerax/
Coot	Emsley et al., 2010	https://www2.mrc-lmb.cam.ac.uk/personal/pemsley/coot/
Origin	Origin Lab Corporation	RRID:SCR_002815
Olympus CellSens	Olympus	RRID:SCR_016238
LabVIEW	National Instruments	RRID:SCR_014325
IMARIS 9.5	Bitplane	RRID:SCR_007370
pClamp 10.7	Molecular Devices	N/A
RStudio	RStudio, Inc.	RRID:SCR_000432
Excel	Microsoft	RRID:SCR_016137
Other		
UltrAuFoil R1.2/1.3 Au 300 mesh	Quantifoil	N1-A14nAu30-01
scRNA-seq database	Tasic et al., 2018	https://portal.brain-map.org/atlases-and-data/rnaseq